# Experimental microwave imaging of three-dimensional targets with different inversion procedures

P. C. Chaumet,[a] K. Belkebir, and A. Sentenac

*Institut Fresnel, Aix-Marseille Université, UMR CNRS 6133, Campus de Saint Jérôme, 13013 Marseille France*

We consider an experimental microwave imaging system in which the targets are illuminated under various angles of incidence and the scattered field is measured on a sphere surrounding them. We estimate the map of relative permittivity of the objects from the scattered field with an iterative inversion procedure based on a conjugate gradient technique. We derive several formulations of the inversion algorithm and analyze their efficiency on three different targets. We observe that including *a priori* information on the lower and upper bounds of the permittivity of the sample leads to a spectacular improvement of the resolution of the image. © *2009 American Institute of Physics.* [DOI: 10.1063/1.3183939]

## I. INTRODUCTION

Wave diffraction tomography is a digital imaging technique in which an unknown object is illuminated by a monochromatic coherent wave under various incident angles and the scattered field is measured in phase and amplitude along various directions of observation. The intrinsic properties (shape, nature) of the object are reconstructed numerically thanks to inversion algorithms accounting for the wave-object interaction. In the last ten years, this approach has stirred a wealth of research in the acoustical, mechanical, and electromagnetic domains and has been studied in the framework of many applications, from nondestructive testing, to detection of buried objects or medical imaging.[1–4] It is also more and more considered in the optical domain as an alternative to classical optical microscopy.[5–7] Performances of wave diffraction tomography depend on the experimental configuration, namely, the number of incidences and observations points, the covered angular range, and the noise level. They also depend on the inversion algorithms that are used for the reconstruction.

Many inversion methods rely on simplified models of the wave-object interaction leading to a linear link between the scattered field and the parameters of interest of the object. Fast techniques such as singular value decomposition,[8] filtered backprojection algorithms,[9] or inverse Fourier transform[6,7] can then be used to solve the linear inverse problem. These methods are restricted to the imaging of certain kinds of samples, such as biological objects in the optical domain. They appear generally inappropriate when the sample supports multiple scattering.[10] Indeed, in this case, the diffracted field is linked to the object intrinsic properties in a complex nonlinear way.

Several teams developed techniques in electromagnetism, for solving these nonlinear and ill-posed problems.[11–14] The most popular approach is to reconstruct the parameter of interest, namely, the permittivity distribution within a bounded region, iteratively. Starting from an initial guess,

which could be either a constant permittivity or deduced from the back-propagation technique,[15] the unknown object is retrieved gradually by minimizing a cost function describing the discrepancy between measurements (data) and scattered fields computed via a forward solver for the best available estimation of the target under test. These nonlinear inversion algorithms have mostly been applied to wave diffraction tomography in the microwave domain.

More recently, similar approaches have been developed specifically for imaging samples in the optical domain with the objective to ameliorate the power of resolution of far-field optical microscopes.[6,16–18] Improvement of the resolution was obtained by optimizing the imager configuration, for example, by illuminating the targets through a prism[7,15,19] or through an optimized periodically nanostructured substrate,[20,21] and also by using nonlinear inversion algorithms instead of linear ones when the sample presents high or moderate permittivity contrast.[15,21] It was shown that accounting for multiple scattering (when it is present) in the inversion procedure can even lead to a better resolution than that expected with the single scattering analysis.[10,22,23] These different studies, which were mostly conducted with synthetic data, stressed the importance of developing sophisticated inversion procedures, especially when one seeks to ameliorate the power of resolution of a given experimental configuration. In this work, we present different inversion methods in electromagnetism and we compare their performances with experimental data obtained in the microwave domain with three-dimensional canonical targets.[24,25] More precisely, we investigate the performances of reconstruction procedures accounting for single or multiple scattering and we investigate the interest of introducing *a priori* information on the permittivity of the sample.

## II. THEORY

### A. Forward scattering problem

The core of an inversion scheme lies in the wave-object interaction model that has been chosen. In this work, we

---

a)Electronic mail: patrick.chaumet@fresnel.fr.

consider a rigorous modeling of the electromagnetic wave scattering based on Maxwell equations. The resolution of these equations is performed with the coupled dipole method (CDM), which was introduced by Purcell and Pennypacker[26] in 1973 for studying the scattering of light by nonspherical dielectric grains in homogeneous space. This technique is equivalent to a volume method of moment.[27] The object under study is represented by a three-dimensional cubic array of $N$ polarizable subunits. The electric field at each subunit position is derived from the self-consistent equation:

$$\mathbf{E}(\mathbf{r}_i) = \mathbf{E}^{\text{inc}}(\mathbf{r}_i) + \sum_{j=1, j \neq i}^{N} \mathbf{T}(\mathbf{r}_i, \mathbf{r}_j) \alpha(\mathbf{r}_j) \mathbf{E}(\mathbf{r}_j), \qquad (1)$$

where $\mathbf{E}^{\text{inc}}(\mathbf{r}_i)$ denotes the incident field at the position $\mathbf{r}_i$, i.e., the total electric field that would be observed in the absence of the scattering object. $\mathbf{T}$ describes the linear response of a dipole in homogeneous space[28] and $\alpha(\mathbf{r}_j)$ is the polarizability of the subunit $j$. According to the Clausius–Mossotti expression, the polarizability distribution $\alpha$ may be written as

$$\alpha(\mathbf{r}_j) = \frac{3d^3}{4\pi} \frac{\varepsilon(\mathbf{r}_j) - \varepsilon_0}{\varepsilon(\mathbf{r}_j) + 2\varepsilon_0}, \qquad (2)$$

where $d$ is the spacing of lattice discretization and $\varepsilon(\mathbf{r}_j)$ is the relative permittivity of the object. The relative permittivity of the homogeneous background medium is denoted by $\varepsilon_0$. This expression of the polarizability corresponds to the weak form of the CDM (Ref. 29) and is accurate enough for the present study. However, in a different topic, such as optical forces analysis[30] or the extinction cross-section modeling,[31] one needs to take into account the radiative reaction term. The material under test is assumed to be isotropic. Hence, the relative permittivity $\varepsilon(\mathbf{r}_j)$ and subsequently the polarizability are both scalars. Once the linear system represented by Eq. (1) is solved, the scattered field $\mathbf{E}^d(\mathbf{r})$ at an arbitrary position $\mathbf{r}$ exterior to the object is given by

$$\mathbf{E}^d(\mathbf{r}) = \sum_{j=1}^{N} \mathbf{T}(\mathbf{r}, \mathbf{r}_j) \alpha(\mathbf{r}_j) \mathbf{E}(\mathbf{r}_j). \qquad (3)$$

The scattered field is collected at $M$ observation points for $L$ successive illuminations. Let $\mathbf{E}_l^d$ be the scattered field corresponding to the $l$th illumination with $l = 1, \ldots, L$. For sake of simplicity Eqs. (1) and (3) are rewritten in a more condensed form:

$$\mathbf{E}_l = \mathbf{E}_l^{\text{inc}} + \overline{\mathbf{A}} \mathbf{p}_l, \qquad (4)$$

$$\mathbf{E}_l^d = \overline{\mathbf{B}} \mathbf{p}_l, \qquad (5)$$

where $\overline{\mathbf{A}}$ is a square matrix of size $(3N \times 3N)$ that contains all the field susceptibilities $\mathbf{T}(\mathbf{r}_i, \mathbf{r}_j)$. The $(3M \times 3N)$ matrix $\overline{\mathbf{B}}$ contains the field susceptibilities $\mathbf{T}(\mathbf{r}_k, \mathbf{r}_j)$, where $\mathbf{r}_j$ denotes a point in the discretized object, $j = 1, \ldots, N$, while $\mathbf{r}_k$ is an observation point, $k = 1, \ldots, M$. The vector $\mathbf{p}_l = \alpha \mathbf{E}_l$ represents the induced dipoles inside the scattering object for the illumination $l$. Note that matrices $\overline{\mathbf{A}}$ and $\overline{\mathbf{B}}$ do not depend on the incident field nor on the object under test.

When the object is weakly scattering (i.e., small enough compared to the wavelength), a common approximation consists in assuming that the field inside the object is close to the incident field: $\mathbf{E}_l = \mathbf{E}_l^{\text{inc}}$. This approximation, known as the Born approximation, amounts to considering only single scattering events. It yields a linear relationship between the scattered field and the polarizability and permits to avoid solving the time-consuming Eq. (4).

## B. Inverse scattering problem

The inverse problem consists in retrieving a parameter of interest linked to the object (map of permittivity, polarizability) from the scattered field. There exists an abundant literature on techniques that solve iteratively the inverse problem, see for instance[13,32] and the references cited therein. It is assumed that the target under test is confined in bounded box $\Omega$ outside of which the parameter of interest is equal to zero. Then, starting from an initial guess, based on the backpropagation technique,[33] the parameter of interest is adjusted gradually by minimizing a cost functional of the form[10,33]

$$\mathcal{F}(\varepsilon) = \frac{\sum_{l=1}^{L} \|\mathbf{f}_l^d - \mathbf{E}_l^d\|^2}{\sum_{l=1}^{L} \|\mathbf{f}_l^d\|^2}, \qquad (6)$$

where $\mathbf{f}_l^d$ is the "experimental" data and $\mathbf{E}_l^d$ is the simulated field radiated with the best available estimated parameter of interest. he minimization of the cost functional is performed numerically thanks to a conjugate gradient algorithm.

In the first inversion procedure considered in this paper, the polarizability is taken as the parameter of interest. We thus build a sequence $\{\alpha_n\}$ according to the following recursive relation:

$$\alpha_n = \alpha_{n-1} + a_n d_n, \qquad (7)$$

where the updated polarizability $\alpha_n$ is deduced from the previous one $\alpha_{n-1}$ by adding a correction. This correction is composed of two terms: a scalar weight $a_n$ and a search direction $d_n$. Once the updating direction $d_n$ is found (this will be specified later in the paper), the scalar weight $a_n$ is determined by minimizing the cost functional $\mathcal{F}_n(\alpha_n)$. At each iteration, the field $\mathbf{E}_{l,n}$ inside the test domain $\Omega$ is assumed to be independent of the parameter of interest. Under the Born approximation, it is taken equal to the incident field. In the general nonlinear case, it is the solution of Eq. (6) with $\alpha_{n-1}$. The simple dependence of $\mathcal{F}_n$ with respect to $\alpha_n$ permits to obtain an analytical expression for $a_n$,

$$a_n = \frac{\sum_{l=1}^{L} \langle \overline{\mathbf{B}} d_n \mathbf{E}_{l,n} | \mathbf{f}_l^d - \overline{\mathbf{B}} \alpha_{n-1} \mathbf{E}_{l,n} \rangle_\Gamma}{\sum_{l=1}^{L} \|\overline{\mathbf{B}} d_n \mathbf{E}_{l,n}\|_\Gamma^2}, \qquad (8)$$

where $\langle \cdot | \cdot \rangle_\Gamma$ denotes the inner product in $L^2$. The updating direction $d_n$ is given by the conjugate gradient direction

$$d_n = g_{n;\alpha} + \gamma_n d_{n-1}, \qquad (9)$$

where $g_{n;\alpha}$ is the gradient of the cost functional $\mathcal{F}$ with respect to the polarizability, assuming that the internal fields $\mathbf{E}_l$ do not change. We find

$$g_{n,\alpha} = -W_{\Gamma}\sum_{l=1}^{L} \mathbf{E}_{l,n}^{*} \cdot \overline{\mathbf{B}}^{\dagger}(\mathbf{f}_l^d - \overline{\mathbf{B}}\alpha_{n-1}\mathbf{E}_l), \tag{10}$$

in which $\mathbf{u}^*$ represents the complex conjugate of $\mathbf{u}$ and $\overline{\mathbf{B}}^{\dagger}$ denotes the transpose complex conjugate matrix of the matrix $\overline{\mathbf{B}}$.

The scalar coefficient $\gamma_n$ is defined as

$$\gamma_n = \frac{\langle g_{n;\alpha} - g_{n-1;\alpha} | g_{n;\alpha}\rangle_{\Gamma}}{\|g_{n-1;\alpha}\|_{\Gamma}^2}. \tag{11}$$

The initial guess of the iterative algorithm $\alpha_0$ is estimated with a back-propagation procedure.[15] Hereafter, we call API the inversion algorithm based on the optimization of the polarizability.

In the second inversion procedure, the parameter of interest is taken equal to the permittivity $\varepsilon$. We thus build a sequence for $\{\varepsilon_n\}$ following the recursive relation

$$\varepsilon_n = \varepsilon_{n-1} + a_n d_n. \tag{12}$$

Finding $a_n$ so that $\varepsilon_n$ minimizes the cost functional $\mathcal{F}$ requires to zero the gradient of $\mathcal{F}$ with respect to the permittivity. The latter can be expressed as

$$g_{n,\varepsilon} = g_{n,\alpha}\frac{d\alpha}{d\varepsilon}. \tag{13}$$

Contrary to the API procedure, there is no analytical expression for the zeros of $g_{n,\varepsilon}$, thus, $a_n$ must be found numerically. The drawback of this additional numerical step that we call EPI procedure is that it slows down the inversion procedure. The advantage is that it is very versatile and can be used for complicated parameters of interest. In particular, if we know that the relative permittivity of the objects under study is real and comprised between 1 and $\varepsilon_r$ we can define a new parameter of interest $\xi$ as $\varepsilon = 1 + (\varepsilon_r - 1)(1 - e^{-\xi^2})$. Then the gradient of $\mathcal{F}$ with respect to $\xi$ is given by

$$g_{n,\xi} = g_{n,\varepsilon}\frac{d\varepsilon}{d\xi}. \tag{14}$$

Following the EPI procedure, we use a numerical optimization scheme to zero $g_{n,\xi}$ and find $a_n$. Hereafter, we call XPI the inversion technique based on the optimization of the parameter $\xi$, respectively.

## III. RESULTS

The experimental data were obtained in the anechoic chamber of the Institut Fresnel, using a HP8510 network analyzer, external mixers, an emitting parabolic antenna Hyptra NE5256, and a receiving ridged horn ARA DRG 118. Due to the parabola bandwidth, the operating frequency is varied only in the range of 3 up to 8 GHz. The incident field polarization is changed by rotating mechanically the emitting parabola, while the total field is measured for only one direction of the receiving antenna. By virtue of the reciprocity theorem, this configuration is equivalent to the complete measurement of the vectorial total field for one incident polarization. The scattered field is obtained by subtracting the measured incident field (without the targets) to the measured total field. 24 h are necessary to collect the data for one
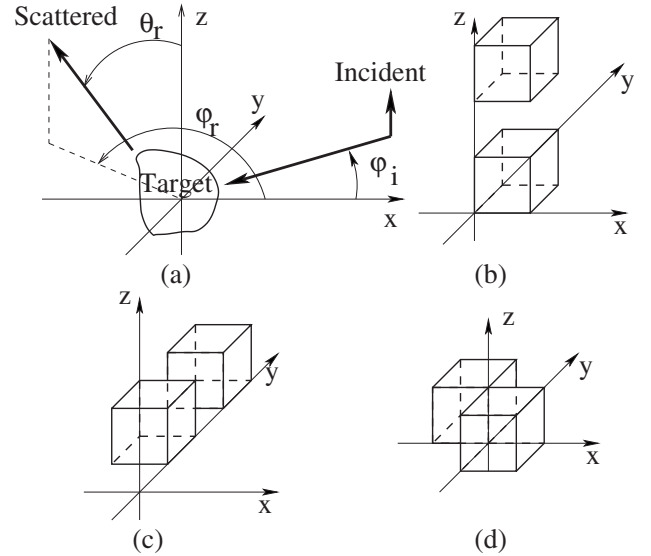


FIG. 1. (a) Sketch of the experimental setup. The illumination is done on the $(x,y)$ plane with $\phi_i$ from 0° to 350° step 10°. The polarization of the incident field is along the $z$ direction. The receiver position $\phi_r$ from 20° to 340° step 40° and $\theta_r$ from 30° to 150° step 15°. (b)–(d) are the three different targets under study: two dielectric cubes of relative permittivity $\varepsilon = 2.4$ and of side size $a = 2.5$ cm located at (b) $(a/2, a/2, a/2)$ and $(a/2, a/2, 5a/2)$, (c) $(a/2, -a/2, 3a/2)$ and $(a/2, 3a/2, 3a/2)$, and (d) $(-a/2, a/2, a/2)$ and $(a/2, -a/2, a/2)$.

target. The drift errors caused by this long delay are corrected following the procedure described in Ref. 34. More details on the experimental configuration can be found in Refs. 24, 35, and 36.

Data calibration is an important issue when dealing with quantitative digital imaging. This is achieved thanks to a reference target and by comparing the measured scattered field to the theoretical one. The measurements were performed in the $(x,y)$ plane in the copolarization configuration. The reference target was a metallic sphere of 70 mm diameter. The simulated field was performed thanks to the Mie theory. A plane wave illumination was assumed in the simulations, which is consistent with the use of a parabolic antenna as source. Details of this calibration procedure is described in Ref. 35.

Figure 1(a) shows the incident and scattered angular ranges: the incident wave is assumed to be a plane wave propagating in the $(x,y)$ plane with $\phi_i$ varying from 0° to 350° with a step of 10°. The polarization of the incident field is along the $z$ direction. The receiver position is defined by $\phi_r$, which varies from 20° to 340° with a step of 40° and $\theta_r$, which varies from 30° to 150° with a step of 15°. The scattered field is recorded for three different frequencies, $f = 3$, 5, and 7 GHz, which correspond to wavelengths of 100, 60, and 43 mm, respectively. The targets are placed in a homogeneous background medium with relative permittivity $\varepsilon_0 = 1$.

We apply the different reconstruction procedures (Born approximation based on API approach, nonlinear API, EPI, and XPI) to three sets of experimental data. The targets under study are made of two cubes of relative permittivity $\varepsilon = 2.4$ and side $a = 25$ mm, the centers of which are separated by 50 mm along the $z$ axis, Fig. 1(b), or along the $y$ axis, Fig. 1(c), or placed along the second bisector of the $(x,y)$ plane so that
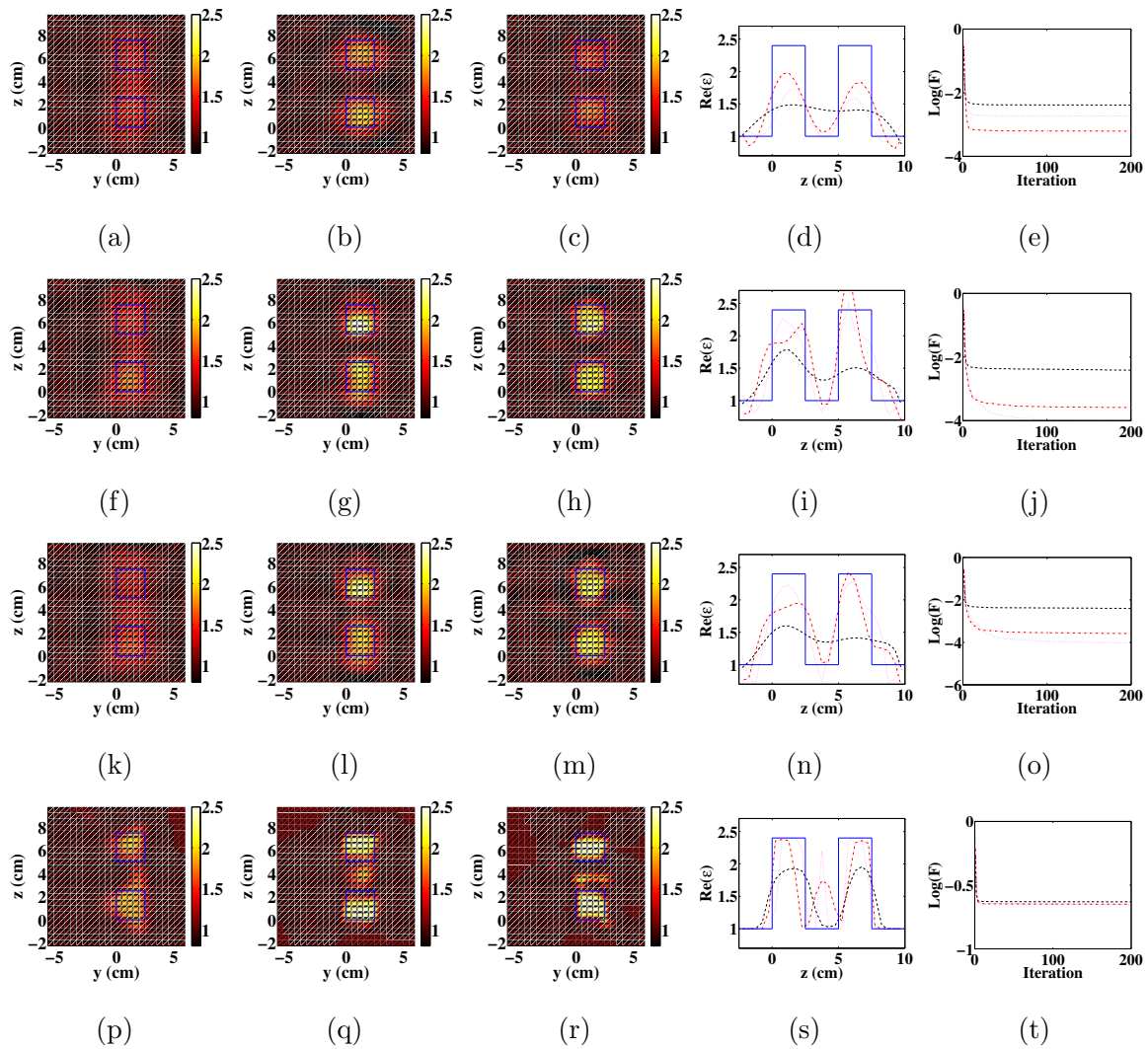
FIG. 2. (Color online) The first row presents the results of our inversion scheme under the Born approximation. The second row uses the nonlinear procedure with the polarizability as the parameter of interest. The third row uses the nonlinear procedure with the relative permittivity as the parameter of interest. The fourth row uses a nonlinear procedure with *a priori* information. The first, second, third column is the map of relative permittivity in the $(y,z)$ plane at $x = a/2$ at $f = 3$, 5, and 7 GHz, respectively. The blue squares depict the actual boundaries of the targets. The fourth column compares the reconstructed real part of the relative permittivity and the actual one along a line crossing the center of the two cubes for 3 (–), 5 (–·), and 7 GHz (···). The solid line is the actual profile. The fifth column displays the evolution of the minimized cost function in log scale, 3 (–), 5 (–·), and 7 GHz (···).

their edges are in contact, Fig. 1(d). Note that the targets presented in Figs. 1(b) and 1(c) are similar except for a rotation of $\pi/2$ about the $x$ axis. These two configurations allow one to investigate the different resolutions along the $z$ or $y$ axis induced by the restriction of the rotation of the incident beam to the $(x,y)$ plane.

For the inversion procedure, we assume that the targets are confined in a bounded box $\Omega$ of size $125 \times 125 \times 125$ mm$^3$. At the operating frequency of 7 GHz, the volume of this bounded box is about 24 $\lambda^3$. The spacing lattice of $\Omega$ is taken equal to $d = 5$ mm whatever the frequency of the data set. We checked that this spacing lattice ensured an accurate calculation of the forward model. The inversion procedure was stopped at the 200th iteration for all the reconstructions. In the following, we present only the real part of the estimated map of permittivity as we observed that the imaginary part is always negligible. In all the plots, the permittivity map is shown in a plane containing the actual two

centers of the cubes and the permittivity profile is drawn along a line joining the actual centers of the cubes.

## A. Analysis of the resolution with the single scattering model

Under the Born approximation, it can be shown easily that the field detected in the **k** direction that is scattered by an object illuminated by a plane wave along the $\mathbf{k}_i$ direction is proportional to the Fourier transform of the object polarizability taken at the spatial frequency $\mathbf{k} - \mathbf{k}_i$.[28] The accessible spatial frequencies provided by the experimental configuration allow one to estimate the expected resolution of the imager. With the chosen incident and detection angular ranges of our experimental setup (see Fig. 1), the boundaries of the accessible spatial frequencies are $[-2k_0, 2k_0]$ in the $(x,y)$ plane and $[-0.9k_0, 0.9k_0]$ along the $z$ axis. Consequently, the expected resolution is about $\lambda/4$ in the $(x,y)$ plane and only $\lambda/1.8$ along the $z$ axis. At 3, 5, and 7 GHz,
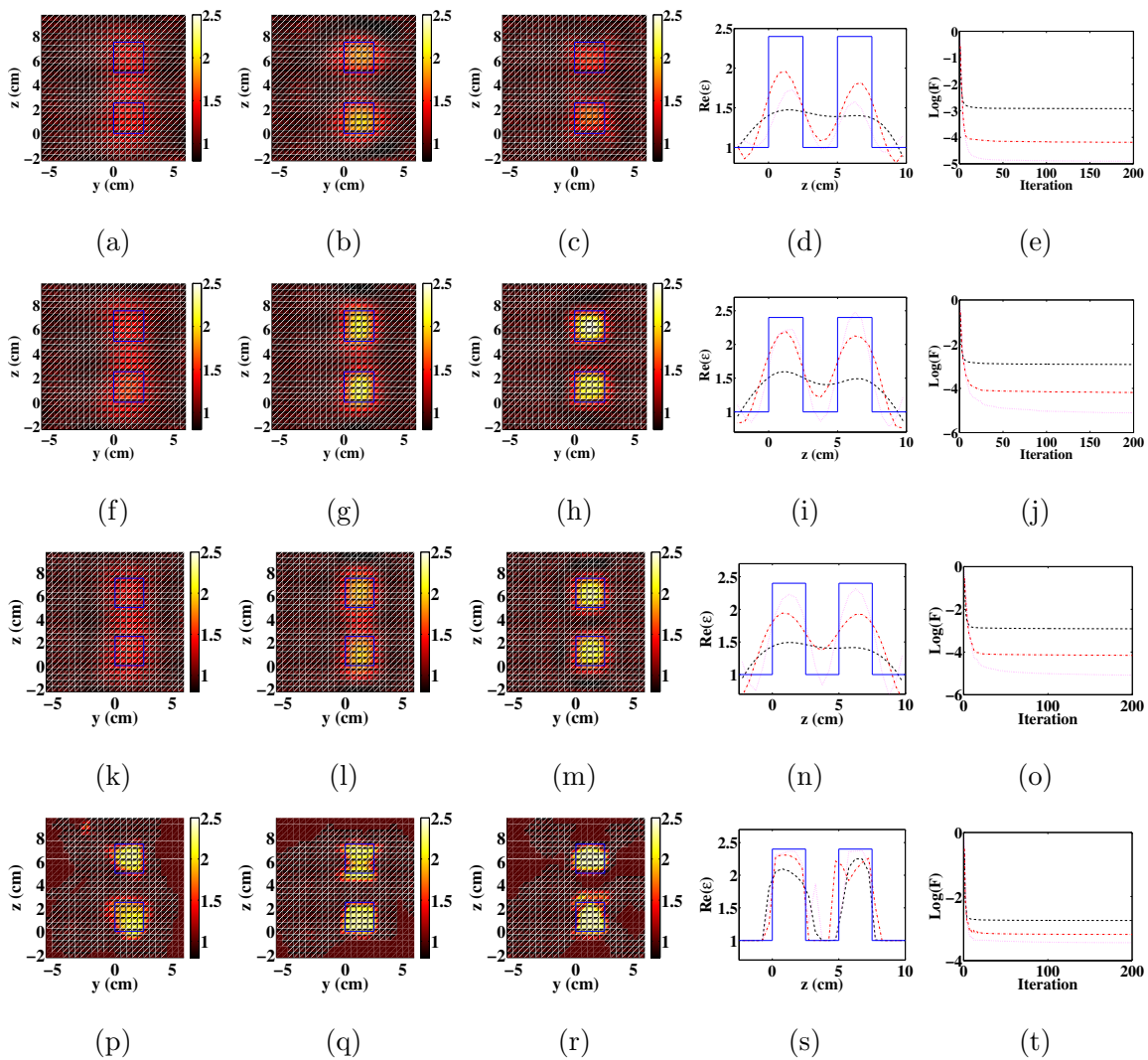
FIG. 3. (Color online) Same caption as in Fig. 2 but solely the copolarized data sets are considered in the inversion procedures.

the resolution is about 25, 15, and 11 mm in the $(x,y)$ plane and 56, 33, and 24 mm along the $z$ axis, respectively.

## B. Two cubes along the *z* direction

In this paragraph, we investigate the resolution of our imager along the $z$ axis, Fig. 1(b). We first analyze the reconstructed maps of permittivity obtained under the Born approximation, Figs. 2(a)–2(d), for the three different frequencies. The evolution of the cost function versus the iteration is presented in log scale in Fig. 2(e). We observe that at the smallest frequency, $f=3$ GHz, i.e., $\lambda=100$ mm, it is not possible to distinguish the two cubes from the images [see the continuous line in Fig. 2(d)]. This lack of resolution is not due to a model error since, at this frequency, the target is small compared to the wavelength and the Born approximation is relatively accurate. It simply stems from the limited resolution of the imager along the $z$ axis (56 mm at 3 GHz) as estimated previously with the single scattering analysis. The distance between the centers of the cubes is 50 mm along the $z$ axis; it is not surprising that the reconstruction fails to distinguish the two cubes. At higher frequencies (5 and 7 GHz), the single scattering analysis indicates that one

could possibly distinguish the two cubes. However, in these cases, the single scattering model becomes inaccurate and the estimated value of the relative permittivity is far from the actual one.

Figures 2(f)–2(o) show the map of permittivity obtained with a nonlinear inversion scheme using either the polarizability (API) or the relative permittivity (EPI) as the parameter of interest. We observe that the two procedures yield similar results. This is certainly due to the fact that, with the dielectric targets under study, there is a relatively small difference between the values of the polarizability and that of the relative permittivity.

At 3 GHz the images obtained with the nonlinear procedure are only slightly better than that obtained under the Born approximation. This result was expected since the single scattering model is a good approximation in this case. At higher frequencies (5 and 7 GHz), the nonlinear inversion procedure yields a more accurate estimation of the permittivity value than that obtained with the Born approximation. On the other hand, the images appear more noisy (for example, the size of the lower cube appears larger than that of the upper one). This result points out the importance of an accu-
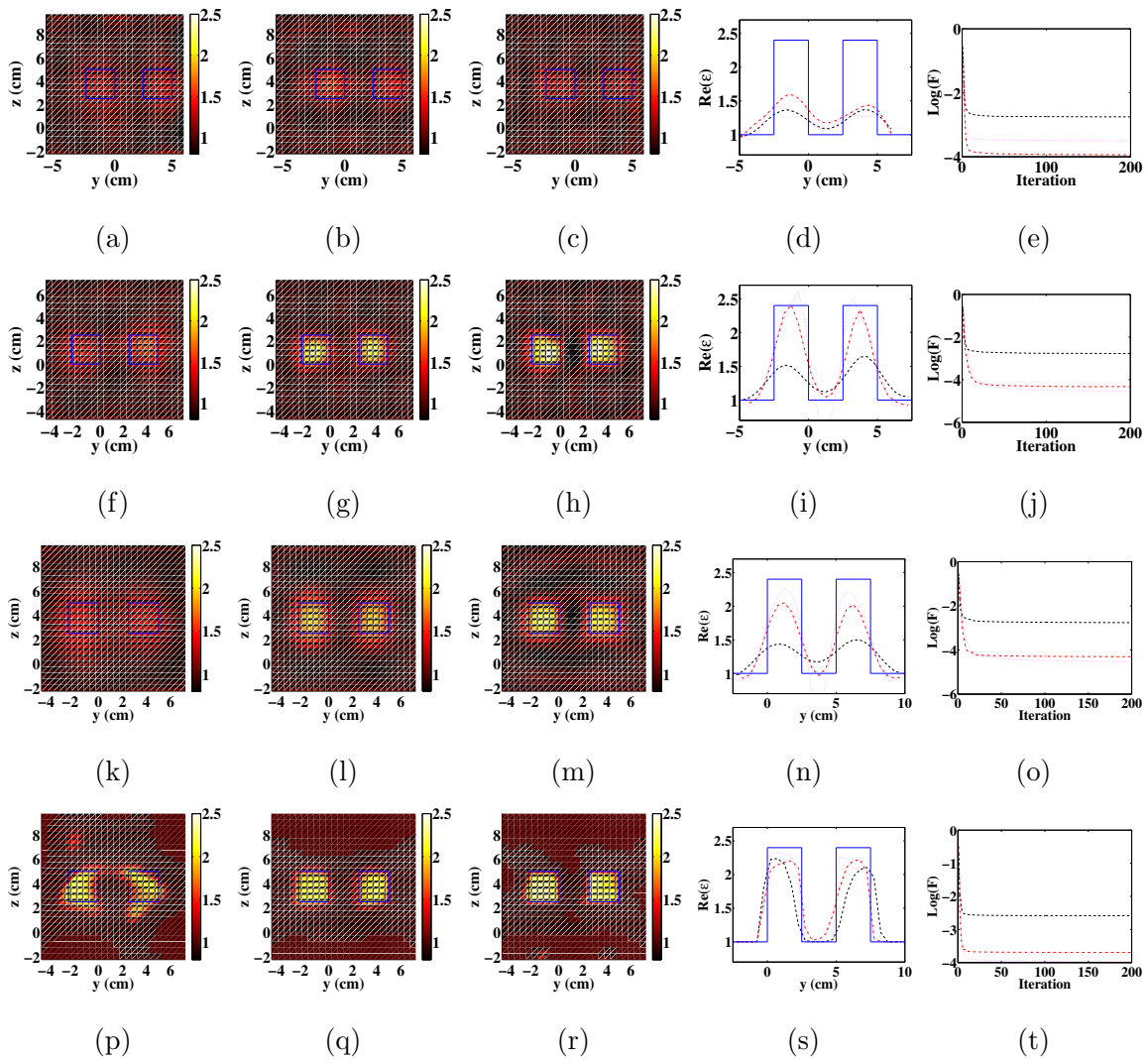
FIG. 4. (Color online) Same caption as in Fig. 3 but the reconstruction of the map of relative permittivity is done in the $(y,z)$ plane at $x=a/2$ and the profile is done for $z=3a/2$ and $x=a/2$.

rate forward model when quantitative imaging is required and it also stresses the increased sensitivity to noise of nonlinear procedures.

In Figs. 2(p)–2(t) we plot the map of permittivity obtained by introducing a strong *a priori* information in the reconstruction procedure: the permittivity is forced to be real and varying within the range [1, 2.4]. We observe that, at the lowest frequency of 3 GHz, it is now possible to distinguish easily the two cubes. This spectacular result demonstrates that the resolution given by the single scattering analysis is not a fundamental limit, (even when the forward single scattering model is valid). The images can be ameliorated in a significant way by introducing *a priori* information. At higher frequencies (5 and 7 GHz), the shape and value of permittivity are improved but the increased sensitivity to noise results in the appearance of spurious peaks of permittivity.

In the previous reconstructions, the experimental data consisted in the measurements of the copolarized and cross-polarized scattered fields. Now, since the targets are relatively small compared to the wavelength, the cross-polarized field component is much weaker than its copolarized coun-

terpart and consequently much noisier. More precisely, we found that the magnitude of the cross-polarized term is at least ten times smaller than that of the copolarized term and that the residue between the experimental data and the field computed for the actual shape of the targets,

$$r = \frac{\sum_{l=1}^{L}\|\mathbf{f}_l^d - \mathbf{E}_l^d\|^2}{\sum_{l=1}^{L}\|\mathbf{E}_l^d\|^2},\tag{15}$$

is always below 0.1 for the copolarized term, while it reaches 4000, 57, and 17 for the cross-polarized component at 3, 5, and 7 GHz, and is about 1 for the total field at all frequencies. Hence, the noise on the data stems essentially from the cross-polarized term. Thus, to diminish the influence of the noise on reconstruction, we decided to discard the data set corresponding to the cross-polarized field. In Fig. 3 we plot the reconstructed map of permittivity that is obtained when sole the copolarized field is accounted for in the inversion.

The reconstruction obtained under the Born approximation with the copolarized field only, Figs. 3(a)–3(e) is similar to that obtained under the Born approximation with the complete set of data, Figs. 2(a)–2(e). This result confirms the
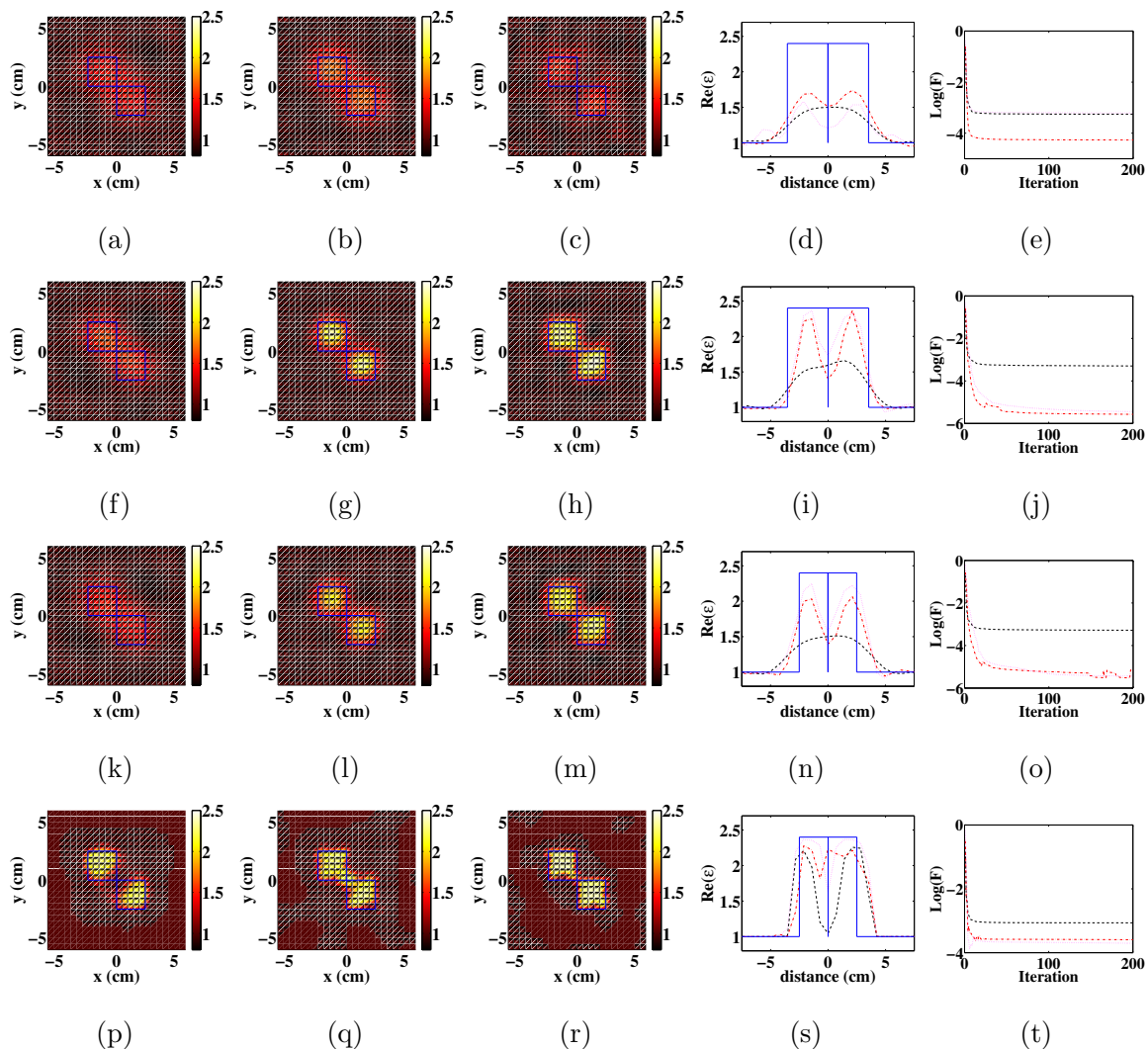
FIG. 5. (Color online) Same caption as in Fig. 3 but the reconstruction of the map of relative permittivity is done in the $(x, y)$ plane at $z = a/2$ and the profile is always done along a line crossing the center of the two cubes hence for $z = a/2$ and $y = -x$.

well-known robustness of any linear inversion to noise. On the contrary, the reconstruction obtained with the nonlinear inversion procedures with and without *a priori* information, Figs. 3(f)–3(t), are much better when the cross-polarized data set is discarded, especially at high frequencies where the previously observed spurious peaks vanish and the same size is obtained for the lower and upper cubes. Hereafter, we will consider only the copolarized data set in the inversion procedures.

### C. Two cubes along the *y* direction

We now investigate the resolution of our imager along the *y* axis, Fig. 1(c), with the four inversion schemes. Contrary to the first configuration, the two cubes can be distinguished on the image obtained under the Born approximation at 3 GHz [Figs. 4(a) and 4(d)]. This result is in agreement with the single scattering analysis that predicts a much better resolution in the $(x, y)$ plane $(\lambda/4)$ than along the *z* axis $(\lambda/1.8)$. In general, all the estimated maps of permittivity plotted in Fig. 4 are more accurate than their counterparts shown in Fig. 3, but the tendency and explanations are similar. In particular, we still observe that introducing *a priori*

information on the permittivity of the target permits to improve spectacularly the reconstruction at all frequencies, and that, at 5 and 7 GHz, it is necessary to use nonlinear inversion procedures to ameliorate the image, Figs. 4(g), 4(h), 4(l), and 4(m).

### D. Two cubes in contact by one edge

In this last paragraph, we consider two cubes placed in the $(x, y)$ plane that are in contact through one edge as depicted in Fig. 1(d). All the tendencies and explanations provided previously can be repeated here. The important point is to note that the center interdistance of the cubes is now 17 mm, i.e., much smaller than the resolution limit provided by the single scattering analysis at 3 GHz (25 mm) and close to that given at 5 GHz (15 mm). Once again, we observe in Fig. 5 that nonlinear inversion algorithms are to be used at 5 and 7 GHz if quantitative information on the relative permittivity is required and that introducing *a priori* information in the inversion procedure permits to overcome the single scattering resolution limit. At the highest frequency, the reconstruction is almost perfect [Fig. 5(r)].

## IV. CONCLUSION

In this work, we investigated the efficiency of different inversion procedures on experimental microwave data. We proposed a linear inversion algorithm based on the Born approximation, a standard nonlinear inversion scheme based on the optimization of the permittivity or the polarizability, and a nonlinear inversion scheme accounting for *a priori* information on the bounds of the permittivity. We analyzed the transverse and axial resolutions of our imager and compared them to those given by a single scattering analysis. We observed that the images provided by the linear inversion algorithm are close to that given by the nonlinear ones at low frequency, when the Born approximation is valid. On the other hand, the nonlinear schemes permit to improve quantitatively and qualitatively the images at higher frequency when multiple scattering becomes important. Yet, they also appear more sensitive to noise. We pointed out that, even though less information are accounted for, discarding the noisy data sets permits to ameliorate the image quality. Last, we have shown that introducing *a priori* information such as bounds on the relative permittivity value in the inversion scheme improves the images in a spectacular way, even at low frequency when the Born approximation is valid. In particular, the resolution of the image can be much better than that given by the single scattering analysis.

[1] A. Dubois, K. Belkebir, and M. Saillard, Inverse Probl. **20**, S63 (2004).
[2] L. Souriau, B. Duchêne, D. Lesselier, and R. E. Kleinman, Inverse Probl. **12**, 463 (1996).
[3] W. Hu, A. Abubakar, and T. M. Habashy, Geophysics **74**, R1 (2009).
[4] S. Semenov, A. Bulyshev, A. Abubakar, V. Posukh, Y. Sizov, A. Souvorov, P. van den Berg, and T. Williams, IEEE Trans. Microwave Theory Tech. **53**, 2284 (2005).
[5] N. Destouches, C. A. Guérin, M. Lequime, and H. Giovannini, Opt. Commun. **198**, 233 (2001).
[6] V. Lauer, J. Microsc. **205**, 165 (2002).
[7] A. Neumann, Y. Kuznetsova, and S. R. Brueck, Opt. Express **16**, 6785 (2008).
[8] P. S. Carney and J. C. Schotland, Opt. Lett. **26**, 1072 (2001).
[9] T. C. Wedberg, J. J. Stamnes, and W. Singer, Appl. Opt. **34**, 6575 (1995).
[10] K. Belkebir, P. C. Chaumet, and A. Sentenac, J. Opt. Soc. Am. A Opt. Image Sci. Vis. **23**, 586 (2006).
[11] A. G. Tijhuis, Wave Motion **11**, 151 (1989).
[12] W. C. Chew and Y. M. Wang, IEEE Trans. Med. Imaging **9**, 218 (1990).
[13] A. Abubakar and P. M. van den Berg, Inverse Probl. **18**, 495 (2002).
[14] C. Yu, M. Yuan, J. Stang, E. Bresslour, R. T. George, G. A. Ybarra, W. T. Joines, and Q. H. Liu, IEEE Trans. Microwave Theory Tech. **56**, 991 (2008).
[15] K. Belkebir, P. C. Chaumet, and A. Sentenac, J. Opt. Soc. Am. A Opt. Image Sci. Vis. **22**, 1889 (2005).
[16] M. Debailleul, V. Georges, B. Simon, R. Morin, and O. Haeberlé, Opt. Lett. **34**, 79 (2009).
[17] S. A. Alexandrov, T. R. Hillman, T. Gutzler, and D. D. Sampson, Phys. Rev. Lett. **97**, 168102 (2006).
[18] K. Belkebir and A. Sentenac, J. Opt. Soc. Am. A Opt. Image Sci. Vis. **20**, 1223 (2003).
[19] P. C. Chaumet, K. Belkebir, and A. Sentenac, Opt. Lett. **29**, 2740 (2004).
[20] A. Sentenac, P. C. Chaumet, and K. Belkebir, Phys. Rev. Lett. **97**, 243901 (2006).
[21] P. C. Chaumet, K. Belkebir, and A. Sentenac, Phys. Rev. A **76**, 013814 (2007).
[22] A. Sentenac, C.-A. Guérin, P. C. Chaumet, F. Drsek, H. Giovannini, N. Bertaux, and M. Holschneider, Opt. Express **15**, 1340 (2007).
[23] F. Simonetti, Phys. Rev. E **73**, 036619 (2006).
[24] J.-M. Geffrin, P. C. Chaumet, C. Eyraud, K. Belkebir, and P. Sabouroux, Appl. Phys. Lett. **92**, 194103 (2008).
[25] P. C. Chaumet and K. Belkebir, Inverse Probl. **25**, 024003 (2009).
[26] E. M. Purcell and C. R. Pennypacker, Astrophys. J. **186**, 705 (1973).
[27] P. C. Chaumet, A. Sentenac, and A. Rahmani, Phys. Rev. E **70**, 036606 (2004).
[28] J. D. Jackson, *Classical Electrodynamics*, 2nd ed. (Wiley, New York, 1975).
[29] A. Lakhtakia, Int. J. Mod. Phys. C **3**, 583 (1992).
[30] P. C. Chaumet, A. Rahmani, and M. Nieto-Vesperinas, Phys. Rev. B **71**, 045425 (2005).
[31] B. T. Draine, Astrophys. J. **333**, 848 (1988).
[32] I. Catapano, L. Crocco, R. Persico, M. Pieraccini, and F. Soldovieri, IEEE Antennas Wireless Propag. Lett. **5**, 49 (2006).
[33] K. Belkebir and M. Saillard, Inverse Probl. **21**, S1 (2005).
[34] C. Eyraud, J.-M. Geffrin, A. Litman, P. Sabouroux, and H. Giovannini, Appl. Phys. Lett. **89**, 244104 (2006).
[35] C. Eyraud, J.-M. Geffrin, P. Sabouroux, P. C. Chaumet, H. Tortel, H. Giovannini, and A. Litman, Radio Sci. **43**, RS4018 (2008).
[36] J. M. Geffrin and P. Sabouroux, Inverse Probl. **25**, 024001 (2009).